International Journal of Hydrogen Energy 46(71): 35137-35148 (2021)
http://dx.doi.org/10.1016/j.ijhydene.2021.08.065 © 2021. This manuscript version is made available under the CC-BY-NC-ND 4.0 license https://creativecommons.org/licenses/by-nc-nd/4.0/

Natural Fe-based catalysts for the production of hydrogen and carbon nanomaterials via methane decomposition

Juliana Alves Silva[a], João Batista Oliveira Santos[a], Daniel Torres[b], José Luis Pinilla[b,*], Isabel Suelves[b]

[a]Departamento de Engenharia Química, Universidade Federal de São Carlos, 13565-905, São Carlos, Brazil

[b]Instituto de Carboquímica-CSIC, Miguel Luesma Castán, 4, 50018, Zaragoza, Spain

Abstract:

Tierga and Ilmenite Fe-based ores are studied for the first time in the catalytic decomposition of methane (CDM) for the production of carbon dioxide-free hydrogen and carbon nanomaterials. Tierga exhibits superior catalytic performance at 800 °C. The effect of the reaction temperature, space velocity and reducing atmosphere in the catalytic decomposition of methane is evaluated using Tierga. The highest stability and activity (70 vol% hydrogen concentration) is obtained at 850 °C using methane as a reducing agent. Reduction with methane causes the fragmentation of the iron active phase and inhibits the formation of iron carbide, improving its activity and stability in the CDM. Hybrid nanomaterials composed of graphite sheets and carbon nanotubes with a high degree of graphitization are obtained. Considering its catalytic activity, the carbon quality, and the low cost of the material, Tierga has a competitive performance against synthetic iron-catalysts for carbon dioxide-free hydrogen and solid carbon generation.

Keywords: catalytic methane decomposition, Tierga iron ore, ilmenite, unsupported Fe catalysts, carbon nanomaterial, hydrogen production.

* Corresponding author: Dr. José Luis Pinilla (jlpinilla@icb.csic.es)

International Journal of Hydrogen Energy 46(71): 35137-35148 (2021)
http://dx.doi.org/10.1016/j.ijhydene.2021.08.065 © 2021. This manuscript version is made available under the CC-BY-NC-ND 4.0 license https://creativecommons.org/licenses/by-nc-nd/4.0/

1. Introduction

Catalytic decomposition of methane (CDM) is recognized as a promising approach for the co-production of CO_2-free H_2 and high value-added carbon nanomaterials (CNMs) [1]. Conventionally, steam methane reforming (SMR) followed by the water-gas shift reaction is one of the most developed processes for large-scale hydrogen generation. Despite the optimizations, SMR is associated with high emissions of CO_2 (ca. 12 t CO_2/t H_2), high capital and operating costs [2]. CDM has the advantage of producing H_2 and high value-added carbon nanostructures in a single step without generating greenhouse gases (Reaction 1). In this regard, the CDM process becomes increasingly cost-competitive when public policies support free taxes or negative costs related to CO_2 yield and the solid carbon has commercial value [3]. The carbon nanostructures formed in this process include mainly carbon nanotubes [4] or nanofibers [5] and in some cases few-layered graphene or graphite nanosheets [6].

$$CH_4(g) \rightarrow C(s) + 2H_2(g),\ \Delta H^0_{25°C} = 75.6\ \text{kJ/mol} \quad (1)$$

Catalysts typically used in the CDM reactions are based on Ni and Fe, with operating temperatures between 500 and 900 °C [7-9]. Although Ni-based catalysts are the most active and stable at temperatures between 500 and 700 °C, it rapidly deactivates with increasing temperature [10,11]. On the other hand, Fe-based catalysts are cheaper and require higher temperatures (700-900 °C) [8,12,13]. This latter range of temperatures provides a positive shift of the thermodynamic equilibrium of the CDM reaction, and thus higher methane conversion may potentially be obtained, as well as an improved structural order in the obtained graphitic nanomaterials [14].

The main steps involved in the CDM reaction are: (1) methane cracking, (2) dissolution and diffusion of carbon through the metal particle, and (3) the supersaturation and subsequent precipitation of carbon for the formation of nanostructured carbon [5]. Although the stages of the formation and growth of carbon for Ni- and Fe-based catalysts are certainly related to common factors, there are some differences. The production of as-grown carbon by CDM for Ni

International Journal of Hydrogen Energy 46(71): 35137-35148 (2021)
http://dx.doi.org/10.1016/j.ijhydene.2021.08.065 © 2021. This manuscript version is made available under the CC-BY-NC-ND 4.0 license https://creativecommons.org/licenses/by-nc-nd/4.0/
catalysts occurs through facet mechanism [15], while for Fe catalysts it is through a complex system of different active phases composed of metallic Fe structures and Fe-C alloys, i.e., Fe_3C, α-Fe, γ-Fe, and their alloys [16]. To the best of our knowledge, no studies have been concerned with the influence of each of these components on the results of catalytic reaction, which is an important aspect of the use of iron-based materials in the CDM reaction [17]. A possible reason for this remains in the difficulty to rationalize the factors that lead to the formation of iron phases and metaphase observed under different reaction conditions and catalysts.

Catalyst deactivation by carbon encapsulation and sintering is the prime challenge found in the CDM process [18]. To promote a longer catalyst lifetime, different metal loadings [19], supports [20], synthesis methods [21], reactor configurations and conditions [22] have been studied. For example, Inaba *et al.* [23] investigated Fe-supported alumina catalyst at different temperatures, CH_4 flow rates, and CO_2 concentrations for the production of carbon nanotubes. CH_4 conversion achieved 60% at temperatures higher than 700 °C. They stated that it was possible to increase stability by decreasing gas velocity. By adding CO_2 in the feedstock, higher temperatures and longer catalytic lifetimes can be obtained. Besides this, the prereduction of iron oxides using H_2 is not mandatory and their reduction can proceed during the CH_4 stream at temperatures higher than 680 °C to provide a sufficiently high and stable conversion.

Expensive catalysts and synthesis methods can compromise the viability of CDM [2]. Depending on the application of the carbon, it is necessary to purify the obtained carbon by removing the metal with acid treatment [4]. An alternative approach is to regenerate the spent catalyst from the CDM by oxidation to reuse the catalyst [24]. In both contexts, Fe-based catalyst is considered suitable for CDM because of its price. Table 1 presents a literature survey on Fe-based catalysts for CDM with their respective reaction conditions and main catalytic results. Table 1 shows that the studies related to CDM mostly use H_2 in the catalyst activation stage; however, from an industrial standpoint, it is desirable to operate with CH_4 in the reduction stage to minimize costs. Enakonda *et al.* [25] studied supported Fe-Al materials for

International Journal of Hydrogen Energy 46(71): 35137-35148 (2021)
http://dx.doi.org/10.1016/j.ijhydene.2021.08.065 © 2021. This manuscript version is made available under the CC-BY-NC-ND 4.0 license https://creativecommons.org/licenses/by-nc-nd/4.0/
CDM evaluating the reducing atmosphere with CH_4 and H_2. Interestingly, the catalytic activity using CH_4 activation was higher than H_2 activation (Table 1). The authors suggested that part of spinel $FeAl_2O_4$ was reduced by H_2, which may result in the sintering of Fe^0 and the lowering of surface area. In contrast, the effect of CH_4 and H_2 gases as a reducer agent on non-supported iron-based material is still poorly known, thus it was thoroughly investigated in this work.

Recently, iron ores have been identified as a promising unconventional catalyst for the CDM reaction to minimize costs [18]. Here, this work explores the use of two different iron ores as catalysts in the production of hydrogen and nanostructured carbon materials via CDM. The iron ores (Tierga and Ilmenite) were chosen because of their low price, wide availability, non-toxicity and catalytic activity in other reactions involving CH_4 [26,27]. Both were subjected to CDM reaction for the first time. Tierga iron ore is mainly composed of Fe_2O_3, and Ilmenite ore contains species of iron and titanium. After the selection of the most active ore (Tierga), several aspects were studied such as reducing atmosphere, reaction temperature and weight hourly space velocity (WHSV) to find an optimal reaction condition providing high catalytic activity and stability. The reduction with CH_4 had a positive impact on the structure of Tierga and the yield of as-deposited nanocarbon mainly at more moderate temperatures. We observed that various types of carbon nanostructures such as graphite-like nanosheets and tubular carbon structures with a high degree of graphitization were obtained over Tierga.

International Journal of Hydrogen Energy 46(71): 35137-35148 (2021)
http://dx.doi.org/10.1016/j.ijhydene.2021.08.065 © 2021. This manuscript version is made available under the CC-BY-NC-ND 4.0 license https://creativecommons.org/licenses/by-nc-nd/4.0/

Table 1 - Data taken from the literature on methane decomposition catalyzed by Fe-based materials.

Catalyst	Iron content	WHSV [L/(g_{cat}.h)]	Reduction Conditions	CDM Conditions	Initial CH_4 conversion	Reaction time (min)	Final CH_4 conversion	Carbon yield (g_c/g_{cat})	Carbon yield (g_c/g_{Fe})	Ref.
Fe-Al	60% Fe	42	10% H_2, 700 °C, 4 h	30% CH_4, 700 °C	58%	60	20%	0.79	1.3	[4]
Fe_2O_3	100% Fe_2O_3	4.5	H_2, 600 °C, 90 min	CH_4, 800 °C	21%	360	30%	0.47	0.67	[14]
Fe–Al	40% Fe	7.5	CH_4, 750 °C	CH_4, 750 °C	66%	120	19%	2.4	6	[25]
Fe–Al	40% Fe	7.5	H_2, 750 °C	CH_4, 750 °C	62%	120	15%	1.91	4.8	[25]
Fe-Ce	27% Fe	4.5	H_2, 700 °C, 90 min	CH_4, 800 °C	35%	360	49%	9.6	35.5	[28]
Fe-La	27% Fe	4.5	H_2, 700 °C, 90 min	CH_4, 800 °C	24%	360	33%	8.95	33.1	[28]
Fe-Mo-Al	62% Fe	1.5	H_2, 750 °C, 1h	CH_4, 750 °C	75%	180	70%	2	3.2	[29]
Fe-Mg	50% Fe	1.5	H_2, 700°C, 2h	CH_4, 700 °C	5%	600	27%	6	12	[30]
Fe–Ce	56% Fe	4	H_2, 750 °C, 3 h	30% CH_4, 750 °C	86%	250	23%	4.07	7.2	[31]
Tierga	52.6% Fe	2	CH_4, 900 °C, 1h	CH_4, 900 °C	67%	180	53%	2.07	3.9	This work
Tierga	52.6% Fe	2	CH_4, 900 °C, 1h	CH_4, 850 °C	41%	180	56%	1.63	3.1	This work
Tierga	52.6% Fe	2	H_2, 900 °C, 1h	CH_4, 800 °C	30%	180	32%	0.82	1.6	This work
Ilmenite	33.3% Fe	2	H_2, 900 °C, 1h	CH_4, 800 °C	8%	180	10%	0.23	0.7	This work

International Journal of Hydrogen Energy 46(71): 35137-35148 (2021)
http://dx.doi.org/10.1016/j.ijhydene.2021.08.065 © 2021. This manuscript version is made available under the CC-BY-NC-ND 4.0 license https://creativecommons.org/licenses/by-nc-nd/4.0/

2. Materials and methods

2.1 Materials

The iron ore that has iron oxide as its main component was named according to its place of origin, Tierga. The other ore containing iron and titanium was called Ilmenite. Tierga was supplied by PROMINDSA (Tierga, Spain) and the Ilmenite by Titania A/S (Sokndal, Norway). The materials were sieved to 200-300 μm, and then used as a catalyst for the CDM reaction without further treatment.

2.2 Techniques of characterization

The crystalline structures of the materials were characterized by X-ray diffraction using a diffractometer Bruker D8 Advance Series 2. The powder XRD patterns were further processed for quantitative and qualitative analysis by applying the Rietveld refinement method (see Supplementary materials). The existence of impurities was determined by inductively coupled plasma optical emission spectrometry (ICP-OES; Ametek Spectroblue). Temperature programmed reduction (TPR-H_2) tests were performed using an AutoChem Analyzer II 2920. TPR-H_2 profiles were acquired using 250 mg of fresh catalyst, under a hydrogen-argon mixture (10% H_2) with a flow rate of 50 mL/min from room temperature to 950 °C using a heating rate of 10 °C/min. N_2 physisorption experiments were analyzed in a Micromeritics Tristar apparatus. The adsorption and desorption of N_2 were determined at −196 °C. Thermogravimetric analysis (TGA) was carried out in a NETZSCH TG 209 F1 Libra thermobalance coupled with the mass spectrometer (MS), OmniStar TM. The sample (ca. 30 mg) was heated from room temperature to 900 °C in a total flow rate of 50 mL/min of methane or hydrogen diluted in argon (10% CH_4 or 10% H_2) using a heat rate of 10 °C/min. Temperature programmed oxidation (TPO) profiles of the carbon were obtained in the same apparatus from room temperature to 900 °C using a heating rate of 10 °C/min, under an air/nitrogen flow rate of 50 mL/min (25:75 vol:vol). The microstructure of the samples was investigated by transmission electron microscopy (TEM, JEOL-2000 FXII). Raman spectra were measured in a Horiba Jobin-Yvon LabRAM HR800 UV spectrometer equipped with a charge-coupled detector. The degree of graphitization of carbon

International Journal of Hydrogen Energy 46(71): 35137-35148 (2021)
http://dx.doi.org/10.1016/j.ijhydene.2021.08.065 © 2021. This manuscript version is made available under the CC-BY-NC-ND 4.0 license https://creativecommons.org/licenses/by-nc-nd/4.0/
was measured using the Raman and XRD results. From the characteristic peaks of carbon from XRD data, it was possible to obtain the interplanar distance (d_{002}) between graphene layers of diffraction peak (002) using the Bragg equation. The graphitization index, g, was calculated using Equation 2 [54]. The layer thickness (L_c) of carbon was calculated by Equation 3, where λ is the X-ray wavelength, B is the angular width of the (002) diffraction peak at half-maximum intensity (radians) and θ is the Bragg angle for reflection (002). The number of graphene layers (n_L) was estimated using Equation 4.

$$g = \frac{0.3440 \quad d_{002}}{0.3440 - \ .3354} \tag{2}$$

$$L_c = \frac{0.89\,\lambda}{B\,\cos\theta} \tag{3}$$

$$n_L = (L_c/d_{002}) + 1 \tag{4}$$

2.3 Catalytic reactions

The catalytic tests were performed in a fixed bed reactor at different pretreatment and reaction conditions. In a typical run, 600 mg of fresh catalyst was reduced from room temperature to 900 °C for 1 h under H_2 or CH_4 flow rate of 1.2 L/h. Then, the CDM reaction was carried out using a pure CH_4 flow rate of 1.2 L/h, at 800, 850, or 900 °C for 3 h. The samples after the reaction were named according to the reducing atmosphere and the reaction temperature. For example, the sample Tierga reduced with H_2 at 900 °C for 1 h was named Tierga-H_2, and after CDM at 850 °C it was named Tierga-$H_2$850. The composition of the exhausted gases was determined by gas chromatography (see Supplementary materials). The CH_4 conversion [X_{CH4}(%)] is given by Equation 5, where $C_{H2} = F_{H2}/F_T \times 100$ is referred to the percentages of the hydrogen content in the exhausted gases and F_{H2} and F_T are the H_2 molar flow rate and total molar flow rate in the reactor output, respectively. The amount of carbon deposited on the catalyst (g_c/g_{cat}) was estimated using Equation 6, where M_c is the carbon molar mass (12.0107 g/mol), V_m is the CH_4 molar volume (22.4 L/mol), Q_{CH4} is the volumetric CH_4 flow rate fed to the reactor (1.2 L/h), and t is the run time (h).

International Journal of Hydrogen Energy 46(71): 35137-35148 (2021)
http://dx.doi.org/10.1016/j.ijhydene.2021.08.065 © 2021. This manuscript version is made available under the CC-BY-NC-ND 4.0 license https://creativecommons.org/licenses/by-nc-nd/4.0/

$$X_{CH_4}(\%) = \frac{C_{H_2}}{200 - C_{H_2}} \times 100 \quad (5)$$

$$g_c = \frac{M_c}{V_m} \int_0^t Q_{CH_4} X_{CH_4} dt \quad (6)$$

3. Results and discussion

3.1 Characterization of fresh Tierga and Ilmenite

Tierga and Ilmenite presented a non-porous structure with surface area of 5.2 and 0.8 m^2/g, respectively. The results of XRD and ICP can be seen in Table 2, Tierga consisted mainly of iron (III) oxide (α-Fe_2O_3; hematite) and Ilmenite of pseudobrookite (Fe_2TiO_5).

Table 2 - Chemical composition (wt. %) of the fresh Tierga and Ilmenite determined by ICP-OES and XRD Rietveld analysis.

	α-Fe_2O_3	Fe_2TiO_5	Others minor phases
Tierga	75.3	-	$CaMg(CO_3)_2$ (11.2), SiO_2 (9), Al_2O_3 (3.3), K_2O (1.0), Na_2O (0.1), TiO_2 (1.0)
Ilmenite	11.2	54.7	TiO_2 (28.6)

The reducibility of these iron ores was studied by TPR-H_2, and its profile is shown in Figure 1. The main peaks were observed in the profile at 440, 690, and 860 °C for Tierga. TPR profiles observed in the literature for unsupported α-Fe_2O_3 materials were analogous to those observed for Tierga [32], which suggested the following global reduction mechanism: α-Fe_2O_3 → Fe_3O_4 → FeO → α-Fe [32]. In Figure 1, the first peak close to 400 °C was related to the transformation of hematite to magnetite, Fe_2O_3 → Fe_3O_4. The existence of peaks above 570 °C in these conditions implied the occurrence of the intermediate FeO phase [32]. After that, the transformation of the Fe_3O_4 phase to metallic Fe between 500 and 900 °C occurred in a two-step magnetite reduction pathway, Fe_3O_4 → FeO → Fe [33].

Four main peaks centered at 430, 620, 920 and 945 °C were observed for Ilmenite in Figure 1. The peak at 430 °C corresponded to the transformation of α-Fe_2O_3 → Fe_3O_4, followed by the stepwise reduction process previously described. The other stages of the reduction of α-

International Journal of Hydrogen Energy 46(71): 35137-35148 (2021)
http://dx.doi.org/10.1016/j.ijhydene.2021.08.065 © 2021. This manuscript version is made available under the CC-BY-NC-ND 4.0 license https://creativecommons.org/licenses/by-nc-nd/4.0/

Fe_2O_3 were overlapped by the changes of Fe-Ti-O. The peak between 500 and 650 °C was attributed to the reduction of: $Fe_3O_4 \rightarrow FeO$, $Fe_2TiO_5 \rightarrow FeTiO_3$ (Reaction 7) and Ilmenite-Fe^{3+} → Ilmenite-Fe^{2+} [34,35]. Peaks above 900 °C were ascribed to the reduction of FeO → Fe and Ilmenite-Fe^{2+} → Ilmenite-Fe^0 [35]. The H_2 consumption of Tierga was five times higher than Ilmenite, 314 and 56 cm^3/g, respectively.

$$Fe_2TiO_5(s) + TiO_2(s) + H_2(g) \leftrightarrow 2FeTiO_3(s) + H_2O(v) \quad (7)$$

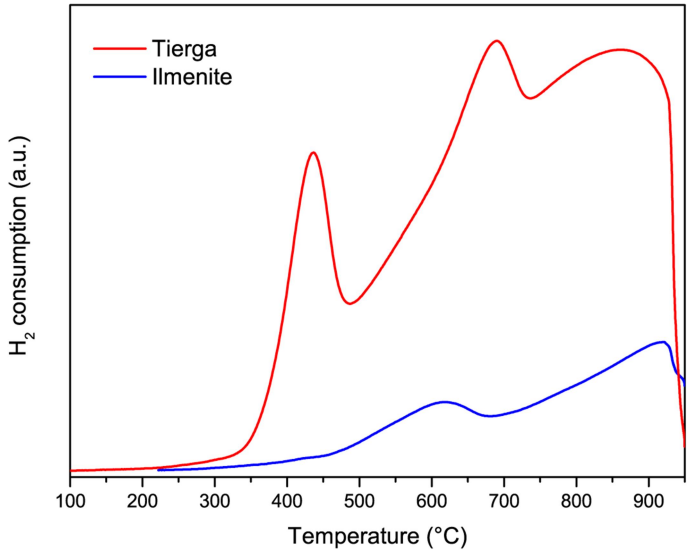

Figure 1 - TPR-H_2 profile of fresh Tierga and Ilmenite.

3.2 Effect of reducing atmosphere

The steps of *in situ* activation with H_2 or CH_4 are the same for iron oxide: α-$Fe_2O_3 \rightarrow Fe_3O_4 \rightarrow FeO \rightarrow$ α-Fe [25]. However, the *in situ* reduction of the catalyst with CH_4 may differ from that with H_2 in the formation of gaseous byproducts throughout the reduction process. By the reduction with CH_4, the formation of traces of CO_x gases is motivated by the reaction between CH_4 and the oxygen of the catalyst from the metal oxide and support [25]. Regarding the properties of the catalyst, it had been pointed out that the reducing agent can modify the type of as-grown carbon [36]. Given these aspects, it is expected that the catalyst undergoes different transformations in particle size, sintering and carbon deposit when reduced with CH_4. The study

International Journal of Hydrogen Energy 46(71): 35137-35148 (2021)
http://dx.doi.org/10.1016/j.ijhydene.2021.08.065 © 2021. This manuscript version is made available under the CC-BY-NC-ND 4.0 license https://creativecommons.org/licenses/by-nc-nd/4.0/
of the reducing atmosphere effect was conducted with Tierga because it has a greater amount of active phase.

3.2.1 Evaluation of the formation of gas byproducts

The evaluation of byproduct formation during the reduction step of Tierga was carried out in a thermobalance using 30 mg and a flow rate of 50 mL/min containing 10% of CH_4 or 10% of H_2 in Ar. The gases evolved were analyzed by mass spectrometry. Figure 2 shows the variation of each gas during the experiment, as well as the sample mass variation and temperature. The appearance of CO and CO_2 mainly occurred at approximately 700 °C for both atmospheres (CH_4 and H_2) due to the decomposition of the dolomite phase that takes place at that temperature [37]. The profile of CO and CO_2 occurred differently between the two pretreatments because an additional formation of CO_x gas was expected from the interaction between CH_4 and catalyst between 600 and 900 °C as aforementioned. Simultaneously, the reduction with CH_4 can lead to other interactions between CH_4 and the byproducts formed during the reduction (H_2O, CO_2, CO, H_2), i.e., the gas-water shift reaction, steam and dry reforming of CH_4. This can be evidenced by the diverse water vapor profiles between CH_4 and H_2 reduction pretreatments. For Tierga pretreated with H_2 (Figure 2-b), the water vapor profile had maximum peaks at 490, 710, and 810 °C, similar to that observed in the TPR-H_2 (Figure 1). However, the water vapor profile for CH_4 reduction pretreatment material had more discrete peaks with maximum peaks at 740 and 880 °C (Figure 2-a), suggesting a CH_4 reforming reaction along the reduction stage as also indicated in another study [38]. Additionally, it is worth mentioning that neither CO nor CO_2 was found at 900 °C for Tierga-H_2 or Tierga-CH_4, in good agreement with the previously reported results [25].

International Journal of Hydrogen Energy 46(71): 35137-35148 (2021)
http://dx.doi.org/10.1016/j.ijhydene.2021.08.065 © 2021. This manuscript version is made available under the CC-BY-NC-ND 4.0 license https://creativecommons.org/licenses/by-nc-nd/4.0/

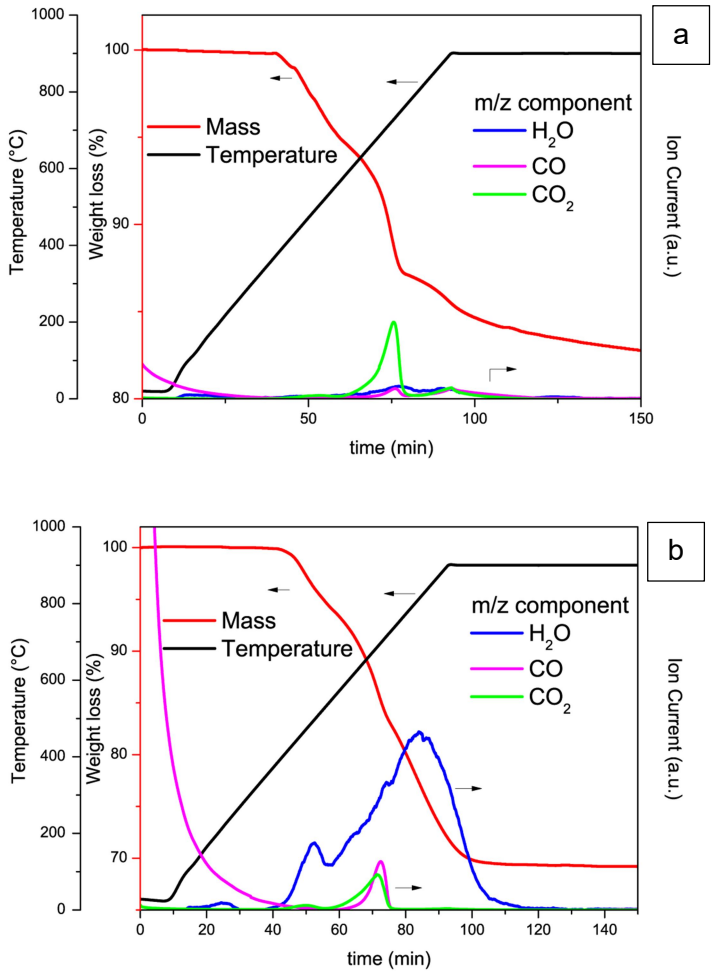

Figure 2 - TGA and MS profiles of reduced Tierga with (a) CH_4 and (b) H_2.

When the reduction with CH_4 was carried out in a fixed bed reactor, the onset of the CH_4 decomposition reaction and the formation of byproducts became more evident (Figure 3). The CH_4 decomposition started after 30 min of reduction at 900 °C as the CH_4 conversion increased abruptly. The profiles of CO and CO_2 were similar to those seen in the experiments using thermobalance (Figure 2-a). The same experiment was not carried out with H_2 at fixed bed because the analysis of gaseous byproducts during the reduction with H_2 had already been verified in Figure 2-b and the CDM reaction proceeds only by contacting methane. According to these reducibility tests, the reduction step for both atmospheres was established up to 900 °C after 1 h. The reduction stage for 1 h at 900 °C is called the activation step hereafter.

International Journal of Hydrogen Energy 46(71): 35137-35148 (2021)
http://dx.doi.org/10.1016/j.ijhydene.2021.08.065 © 2021. This manuscript version is made available under the CC-BY-NC-ND 4.0 license https://creativecommons.org/licenses/by-nc-nd/4.0/

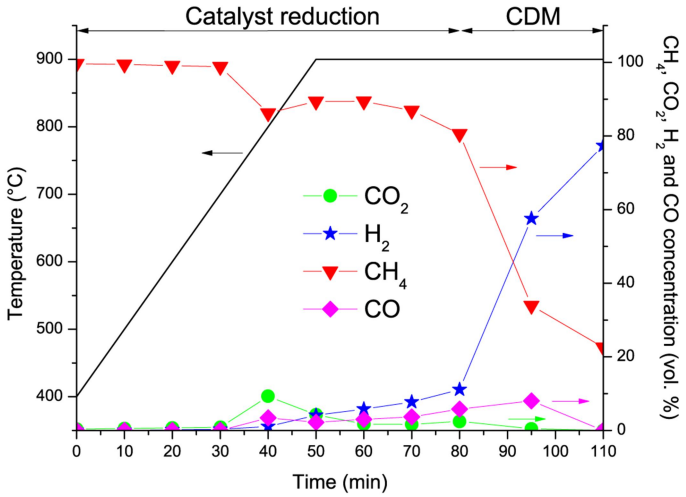

Figure 3 - CH_4, H_2, CO_2 and CO profiles of Tierga reduced with CH_4 in a fixed bed reactor.

3.2.2 Characterization after activation

XRD patterns for Tierga pretreated with H_2 or CH_4 at 900 °C for 1 h are shown in Figure 4. Both materials presented characteristic peaks of the α-Fe phase (ICSD 64998), SiO_2 (ICSD 42498) and new peaks regarding CaO (ICSD 673084) and MgO (ICSD 88058) phases resulting from the decomposition of dolomite. The absence of iron oxides peaks indicated the complete reduction to α-Fe. Fe_3C (ICSD 064689) and graphite (ICSD 76767) were also identified in Tierga-CH_4, suggesting that the CDM reaction started during the reduction step with CH_4. In fact, Zhou *et al.* [33] demonstrated that CDM starts with the formation of Fe_3C and graphite simultaneously on the surface of α-Fe through the reaction between Fe and CH_4 (Equation 8). As soon as Fe_3C is formed, it acts as a catalyst and promotes the methane decomposition into H_2 and carbon [33]. The carbon diffuses into Fe_3C to form supersaturated Fe_3C_{1+x}, which is unstable and immediately decomposes back to stoichiometric Fe_3C and graphite carbon [33].

$$3Fe\ (s) + 2CH_4\ (g) \leftrightarrow Fe_3C\ (s) + C\ (s) + 4H_2\ (g) \quad (8)$$

The concentration and mean crystallite size of α-Fe depended on the pretreatment performed. The percentage of the α-Fe phase in Tierga-H_2 and Tierga-CH_4 catalysts were 85 and 73 wt.%, respectively. The lower concentration of this active phase in Tierga-CH_4 was

International Journal of Hydrogen Energy 46(71): 35137-35148 (2021)
http://dx.doi.org/10.1016/j.ijhydene.2021.08.065 © 2021. This manuscript version is made available under the CC-BY-NC-ND 4.0 license https://creativecommons.org/licenses/by-nc-nd/4.0/

explained by the transformation of this phase into Fe_3C. Moreover, the mean crystallite size of α-Fe in the Tierga treated with H_2 (80 nm) was bigger than the iron ore activated by CH_4 (46 nm), which indicated the fragmentation of the α-Fe phase in Tierga-CH_4 into smaller crystals by the adjacent formation of iron carbide and graphite as previously reported in other catalysts [39,40]. Another possibility involved the effect of Fe_3C and carbon on the catalyst activity. From literature, the iron carbide and carbon can act as textural promoters and prevent the sintering of α-Fe particles, positively impacting in the catalytic activity, as already reported for Ni-based materials during CDM above 500 °C [41]. To confirm this hypothesis and to probe in more detail the ability of these structures to act as promoters in Tierga, different temperatures were used in the reaction (see section 3.3.3). Other works also report that the reduction with H_2 is more severe and leads to larger crystallite sizes by sintering [42]. Once the catalyst is reduced along the activation stage, the reaction step proceeds.

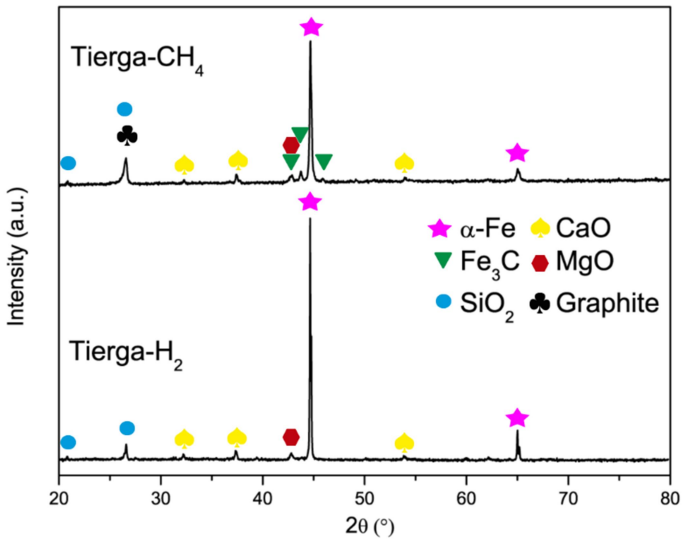

Figure 4 - XRD patterns of the activated Tierga catalysts.

3.3 Activity in the CDM

3.3.1 Preliminary activity over Tierga and Ilmenite

After pure H_2 prereduction at 900 °C for 1 h, Tierga and Ilmenite were subjected to a reaction with pure CH_4 at 800 °C. Figure 5 shows the profiles of the samples in terms of H_2 production (left y axis) and CH_4 conversion (right y axis) during the reaction. Only H_2 and CH_4

International Journal of Hydrogen Energy 46(71): 35137-35148 (2021)
http://dx.doi.org/10.1016/j.ijhydene.2021.08.065 © 2021. This manuscript version is made available under the CC-BY-NC-ND 4.0 license https://creativecommons.org/licenses/by-nc-nd/4.0/
gases were detected during the reaction. The catalytic activities of both declined with time on stream, and after 1 h it increased. A more detailed discussion of this behavior was made in section 3.3.3. Due to the lower Fe loading and higher reduction temperature of the Fe-Ti-O structures, Ilmenite exhibited worse catalytic activity than Tierga in terms of H_2 concentration ranged from 15 to 18%, than those of Tierga with 46-47%. The CH_4 conversion ranged from 8 to 10% for Ilmenite, and 30 to 32% for Tierga. Tierga produced a high carbon yield at 800 °C (0.82 g_c/g_{cat} and 1.6 g_c/g_{Fe}), indicating that is a promising natural catalyst to be used in CDM and, consequently, it was conducted to further experiments.

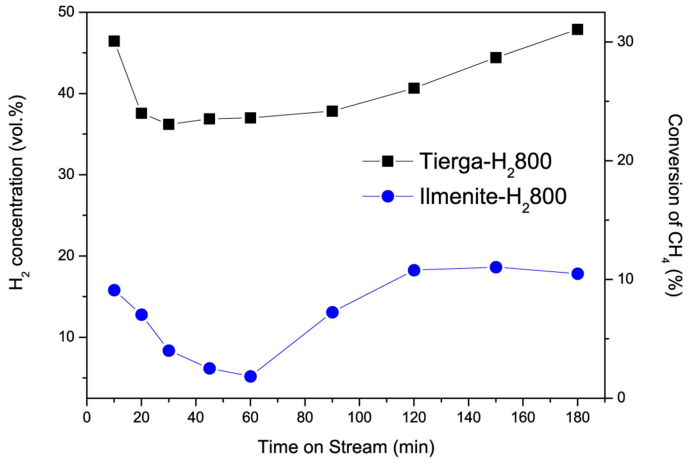

Figure 5 - H_2 concentration and CH_4 conversion evolutions for Tierga and Ilmenite in the CDM reaction at 800 °C. WHSV = 2 L/(g_{cat}·h).

3.3.2 Effect of the WHSV

The influence of the space velocity at 850 °C, with CH_4 activation, and WHSV ranging from 2 to 6 L/(g_{cat}·h) was evaluated and the corresponding H_2 concentration and CH_4 conversion evolutions over Tierga catalyst are shown in Figure S1. With decreasing the space velocity, there was a gain in contact time and consequently, an increase in conversion. The H_2 content profile slightly rose for a WHSV of 2 L/(g_{cat}·h). When increasing the WHSV to 4 and 6 L/(g_{cat}·h), the catalyst underwent a deactivation process after 1 h of reaction. The trend of the WHSV of 2 L/(g_{cat}·h) will be described in detail in the following section.

International Journal of Hydrogen Energy 46(71): 35137-35148 (2021)
http://dx.doi.org/10.1016/j.ijhydene.2021.08.065 © 2021. This manuscript version is made available under the CC-BY-NC-ND 4.0 license https://creativecommons.org/licenses/by-nc-nd/4.0/

3.3.3 Effect of temperature

The effect of the operating temperature on Tierga-CH_4 and Tierga-H_2 activities was evaluated at 800, 850 and 900 °C using WHSV = 2 L/(g_{cat}·h). H_2 concentration and CH_4 conversion changes are shown in Figure 6-a. A significant increase in the amount of produced H_2 was obtained with rising temperature for both catalysts: Tierga-H_2 and Tierga-CH_4. According to literature, the amount of produced H_2 by CDM increases as the temperature increases and the pressure falls [7]. High H_2 concentration (70%) and no deactivation were observed for Tierga-H_2 and Tierga-CH_4 at 850 °C. At 800 °C stable conversion was observed for the catalyst treated with H_2 during about 100 min, followed by slowly rose to 32%, while the CH_4 conversion increased from 24 to 40% after 3 h of reaction for the catalyst treated only with CH_4. At 900 °C, although it exhibited the highest initial catalytic activity, there was a slight deactivation after the first hour of reaction for both Tierga-CH_4 and Tierga-H_2 (ca. 10% H_2 decay). The decrease in the catalytic activity of Tierga-$CH_4$900 and Tierga-$H_2$900 after 1 h can be primarily assigned to the encapsulation of the active phase.

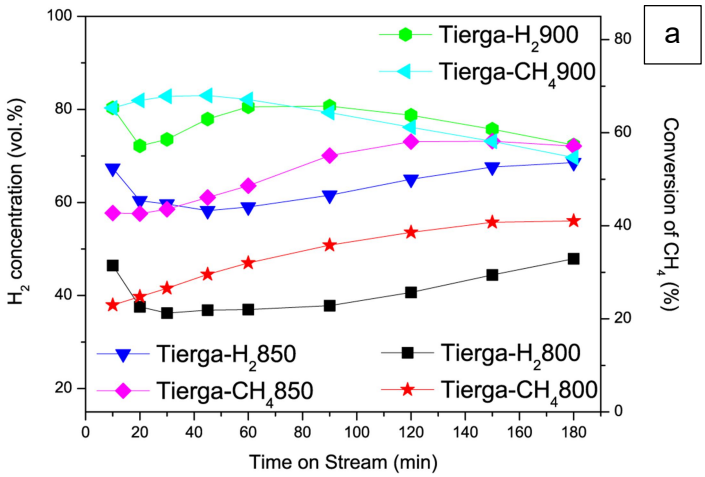

International Journal of Hydrogen Energy 46(71): 35137-35148 (2021)
http://dx.doi.org/10.1016/j.ijhydene.2021.08.065 © 2021. This manuscript version is made available under the CC-BY-NC-ND 4.0 license https://creativecommons.org/licenses/by-nc-nd/4.0/

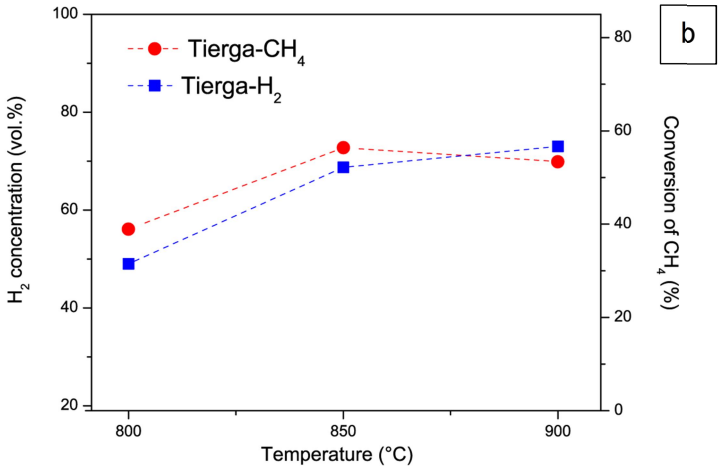

Figure 6 - a) H_2 concentration and CH_4 conversion evolutions for Tierga-CH_4 and Tierga-H_2 in the CDM reaction at 800, 850, and 900 °C; b) H_2 concentration and CH_4 conversion for Tierga-CH_4 and Tierga-H_2 after 3 h of CDM. WHSV = 2 L/(g_{cat}.h).

The early period of catalytic activity, immediately before the period of constant carbon growth, is commonly named the induction period. This step in CDM is usually associated with carbon migration and saturation in catalysts, and metal reconstruction [15]. In Figure 5 and 6-a, the samples Ilmenite-$H_2$800 and Tierga-H_2 (at 800, 850 and 900 °C) showed an initial drop of H_2 production and CH_4 conversion between 10 and 50 minutes. This fall may be related to the period necessary for carbon supersaturation of α-Fe and Fe_3C to take place. Such induction period tended to decrease with rising temperature over Tierga (Figure 6-a). After carbon supersaturation, carbon precipitation occurs. Regarding Tierga-CH_4, the active structures were already partially saturated and therefore had an increasing trend of catalytic activity. The low initial concentrations of Fe_3C and graphite were not sufficient to make these catalysts act as a structural promoter at the beginning of the reaction. As there was an increase in the concentration of Fe_3C and carbon, they could act as support and possibly explain the high stability at 800 and 850 °C.

Figure 6-b summarizes the amount of formed H_2 and the conversion of CH_4 after 3 h of reaction as a function of temperature. The final conversion of CH_4 at 800 °C was about 35% for Tierga-H_2 and Tierga-CH_4. At higher temperatures, the conversion was close to 56% and it was

International Journal of Hydrogen Energy 46(71): 35137-35148 (2021)
http://dx.doi.org/10.1016/j.ijhydene.2021.08.065 © 2021. This manuscript version is made available under the CC-BY-NC-ND 4.0 license https://creativecommons.org/licenses/by-nc-nd/4.0/

independent on the treatment of Tierga. This result revealed that the initial fragmentation and previous saturation with carbon observed in the XRD pattern (Figure 4) had a positive impact on the catalytic results mainly at 800 and 850 °C after 3 h of reaction. Such initial catalyst fragmentation with CH_4 may have brought about the inhibition of agglomeration and sintering of iron-based materials. This disaggregation likely led to greater exposure of the active phase which resulted in higher catalytic activity for Tierga-CH_4 catalyst, as other authors previously reported [43].

Table 3 - Carbon formation and structural parameters for Tierga catalysts after CDM for 3 h at different temperatures.

	Tierga-$H_2$800	Tierga-$CH_4$800	Tierga-$H_2$850	Tierga-$CH_4$850	Tierga-$H_2$900	Tierga-$CH_4$900
g_c (g_c/g_{cat})[a]	0.82	1.05	1.49	1.63	2.04	2.07
d_{002} (nm)	0.3373	0.3374	0.3368	0.3376	0.3369	0.3366
g [b]	0.78	0.77	0.84	0.74	0.83	0.86
L_c (nm)[c]	18.55	17.30	20.85	20.77	20.47	21.24
n_L	56.1	52.4	63.3	63.0	61.8	64.1
I_D/I_G	0.25	0.19	0.23	0.25	0.22	0.21

[a]Carbon yield (Equation 6).

[b]Graphitization degree (Equation 2).

[c]The layer thickness of carbon (Equation 3).

The amount of deposited carbon from these CDM experiments is shown in Table 3. Despite the slight difference between the results for the same temperature, the carbon formation was favored with CH_4 as the reducing agent and with rising temperature. Comparing the carbon yield of Tierga with data taken from the literature (Table 1) is a non-trivial task owing to the diversity of experimental systems. In some cases, Tierga has superior performance than iron-based synthetic catalysts (e.g., 100% Fe_2O_3), which contribute to boosting the competitiveness of Tierga iron ore to reach a commercial level. On the other hand, Tierga material displayed inferior carbon yield than other ones possibly due to an absence of support and a small number of alkaline impurities such as potassium and sodium (Table 2) as previously reported [20]. The experimental conditions used in this work and the results obtained for Tierga without H_2

International Journal of Hydrogen Energy 46(71): 35137-35148 (2021)
http://dx.doi.org/10.1016/j.ijhydene.2021.08.065 © 2021. This manuscript version is made available under the CC-BY-NC-ND 4.0 license https://creativecommons.org/licenses/by-nc-nd/4.0/
pretreatment could be considered as a good advantage for industrial application. In addition, Tierga presents other advantages such as low-cost and high Fe loading.

3.4 Characterization of spent Tierga catalysts

Figure S2 shows the diffractograms of the Tierga catalysts after the reaction. The spent catalysts were composed mostly of α-Fe (ICSD 64998), γ-Fe (ICSD 185721), Fe_3C (ICSD 064689) and graphite (ICSD 76767) phases in all samples except for Tierga-$H_2$800 sample that did not have the pattern of γ-Fe. The as-deposited carbon presented d_{002} values between 0.3376 and 0.3366 nm and g_p between 0.74 and 0.86, respectively (Table 3), i.e., parameters close to the perfect single crystal of graphite structure, which is 0.3354 nm and g_p close to 1. The characterization of carbon by XRD indicated the formation of graphite-like materials with L_c between 17 and 21 nm and a number of graphene layers (n_L) between 52 and 64. Due to the low carbon formation over Ilmenite (0.3 g_c/g_{cat}), only Tierga catalysts were characterized after CDM.

Most samples after the reaction were composed of the γ-Fe structure. This phase is less characterized experimentally due to its instability at temperatures below the boiling point (727 °C). γ-Fe can be an intermediate phase in the production of Fe_3C and graphite at high temperatures [44]. The α-Fe (body-centered cubic system) and γ-Fe (face-centered cubic system) phases have a great affinity with carbon, which allows the dissolution of carbon atoms in the network of these metals, reaching a maximum of 0.022% wt. of C at 740 °C for α-Fe, and 2.14% wt. of C at 1150 °C for γ-Fe. The diffractogram of γ-Fe without carbon saturation found in the literature (ICSD 41506) had peaks at 2θ = 45.8, 53.4 and 78.9°; however, the peaks at 2θ = 43.8, 50.9, 74.9° presented in Figure S2 can be attributed to γ-Fe saturated with carbon (ICSD 185721) [45,46]. This is because γ-Fe allows the insertion of carbon in the interstices of the crystalline network. The rearrangement decreases part of the associated metal-metal energy and changes the diffraction lines of γ-Fe metal to lower angles, as observed for Tierga. Similar results have been reported in earlier publications [45,46]. The carbon-saturated γ-Fe phase was observed only after reaction (Figure S2), and not in the initial activation step (Figure 4), which

International Journal of Hydrogen Energy 46(71): 35137-35148 (2021)
http://dx.doi.org/10.1016/j.ijhydene.2021.08.065 © 2021. This manuscript version is made available under the CC-BY-NC-ND 4.0 license https://creativecommons.org/licenses/by-nc-nd/4.0/
suggests that enough carbon was formed during the reaction to protect and stabilize this intermediate phase.

Based on the XRD data, the iron-based phases were quantified by Rietveld refinement (Figure 7). The amount of Fe_3C decreased with increasing temperature, while iron species increased. The most striking variation in the final composition of the iron phase between the materials took place at 800 °C: Fe_3C was the major product in Tierga-$H_2$800, while α-Fe and γ-Fe become dominant in Tierga-$CH_4$800. However, this difference between the catalysts gradually decreased up to 900 °C. These results indicated that the characteristics of the catalyst after diverse activation atmospheres led to distinct reaction mechanisms at moderate temperatures motivated by the generation of iron phases with distinct crystal systems and fractions.

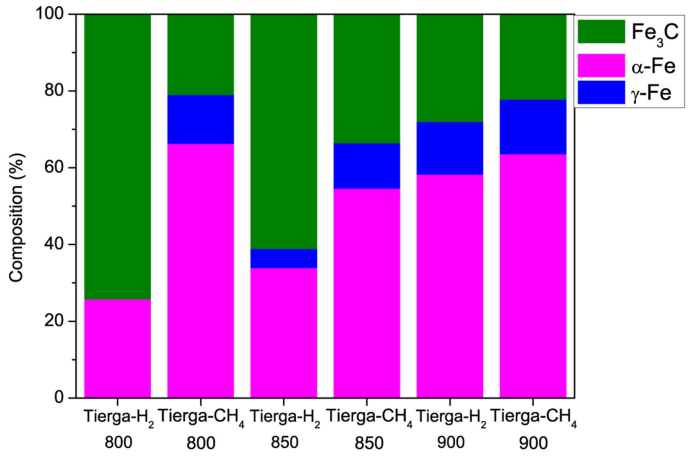

Figure 7 - Iron phase fractions in spent Tierga catalysts by Rietveld refinement of the corresponding XRD patterns (shown in Figure S2).

The most widely reported reaction mechanism is based on the transformation of α-Fe into Fe_3C and graphite (Equation 8). In contrast, previous studies have shown that the mechanism of carbon formation from α-Fe can vary according to the concentration [47] and crystallite size [45] of the α-Fe phase in reactions performed at the same temperature. Wirth *et al.* [47] revealed that depending on the concentration of α-Fe in a temperature range close to the

International Journal of Hydrogen Energy 46(71): 35137-35148 (2021)
http://dx.doi.org/10.1016/j.ijhydene.2021.08.065 © 2021. This manuscript version is made available under the CC-BY-NC-ND 4.0 license https://creativecommons.org/licenses/by-nc-nd/4.0/
eutectic temperature (700-800 °C), γ-Fe or Fe_3C can be obtained, the latter would give rise to carbon. While for Takenaka *et al.* [45], the α-Fe structure was transformed into Fe_3C or γ-Fe depending on the crystallite size of iron oxide. The supported Fe_2O_3 crystallites with smaller sizes were transformed into Fe_3C, while larger ones were transformed into γ-Fe saturated with carbon atoms [45]. Based on these studies, it became evident that for Tierga with reaction taking place at 800 °C (close to the eutectic point), Fe_3C nucleation was favored when the active phase of the catalyst was mainly composed of α-Fe with larger crystallite size, i.e., Tierga-H_2 catalysts. Yet at 800 °C, the γ-Fe phase was preferably promoted by a system with a lower concentration of α-Fe and smaller average crystallite size (Tierga-CH_4 catalysts). As the reaction temperature overpassed the eutectic point towards higher temperatures for other catalysts (Tierga-$CH_4$850, Tierga-$H_2$850, Tierga-$CH_4$900 and Tierga-$H_2$900), there was a higher tendency to promote the nucleation of γ-Fe [47]. Once α-Fe, γ-Fe, or Fe_3C appeared, the carbon dissolution begins to happen and when it reaches the supersaturation of carbon in the metal and/or carbide, the precipitation and growth of carbon occur.

Correlating the XRD results with the catalytic tests for Tierga-$CH_4$800 and Tierga-$H_2$800 it was possible to evaluate the effect of the different active phases (α-Fe, γ-Fe and Fe_3C) on the conversion and H_2 production. The concentration of 55% H_2 (v/v) was obtained in CDM after 3 h for Tierga-$CH_4$800. As Tierga-$CH_4$800 was composed mainly of α- and γ-Fe at the end of the reaction, it seems to indicate that α- and γ-Fe phases were more effective catalysts than Fe_3C. A possible explanation for these results may be that the carbide requires a higher amount of carbon for supersaturation than the metal, maximum of 6.67% wt. of C for Fe_3C [17]. While α-Fe and γ-Fe require a lower amount of carbon for graphite precipitation to occur, usually less than 3% wt. of C [17]. In addition, the carbide bulk diffusion coefficient is lower than that of the metals γ-Fe and α-Fe, implying a higher difficulty in precipitating graphite using carbide [48]. Thus, the mitigation of carbide formation resulted in greater activity of the catalyst, and it was achieved by changing the activation atmosphere to CH_4. As seen in the XRD results, the

International Journal of Hydrogen Energy 46(71): 35137-35148 (2021)
http://dx.doi.org/10.1016/j.ijhydene.2021.08.065 © 2021. This manuscript version is made available under the CC-BY-NC-ND 4.0 license https://creativecommons.org/licenses/by-nc-nd/4.0/
activation with CH_4 led to the initial fragmentation of the α-Fe phase and inhibition of large amounts of Fe_3C.

Figure 8 shows the TEM images of the as-grown carbon from Tierga with different pretreatments and CDM reaction conditions. TEM images confirmed as-deposited carbon in all spent Tierga in the form of carbon nanomaterials (CNMs) with a high degree of graphitization (d_{002} = 3.35 Å), including multi-layered graphene, graphite nanosheets (GNSs) and carbon nanofilaments. The nanofilaments were multi-walled carbon nanotubes and chain-type carbon nanofibers.

In all samples, the GNSs structures (marked with white dotted rectangles) appeared in higher quantities. Generally, they were transparent, rippled graphene/graphite layers, and disengaged from the metallic particles (Figure 8-a, c). Tubular structures (marked with black dotted rectangles) were sparser and shorter, without (Figure 8-f) and with (Figure 8-g) encapsulated iron-based nanoparticles. The chain-type carbon nanofibers (Figure 8-g) had multiple graphite walls around the metal, similar to those observed in previous works with Fe [23]. The metallic particles in the images were round and covered with a thin layer of graphite (Figure 8-c). As the temperature increased, the agglomeration of the metal particles increased (Figure 8-e) as well as the number of metal particles within the chains (Figure 8-f).

International Journal of Hydrogen Energy 46(71): 35137-35148 (2021)
http://dx.doi.org/10.1016/j.ijhydene.2021.08.065 © 2021. This manuscript version is made available under the CC-BY-NC-ND 4.0 license https://creativecommons.org/licenses/by-nc-nd/4.0/

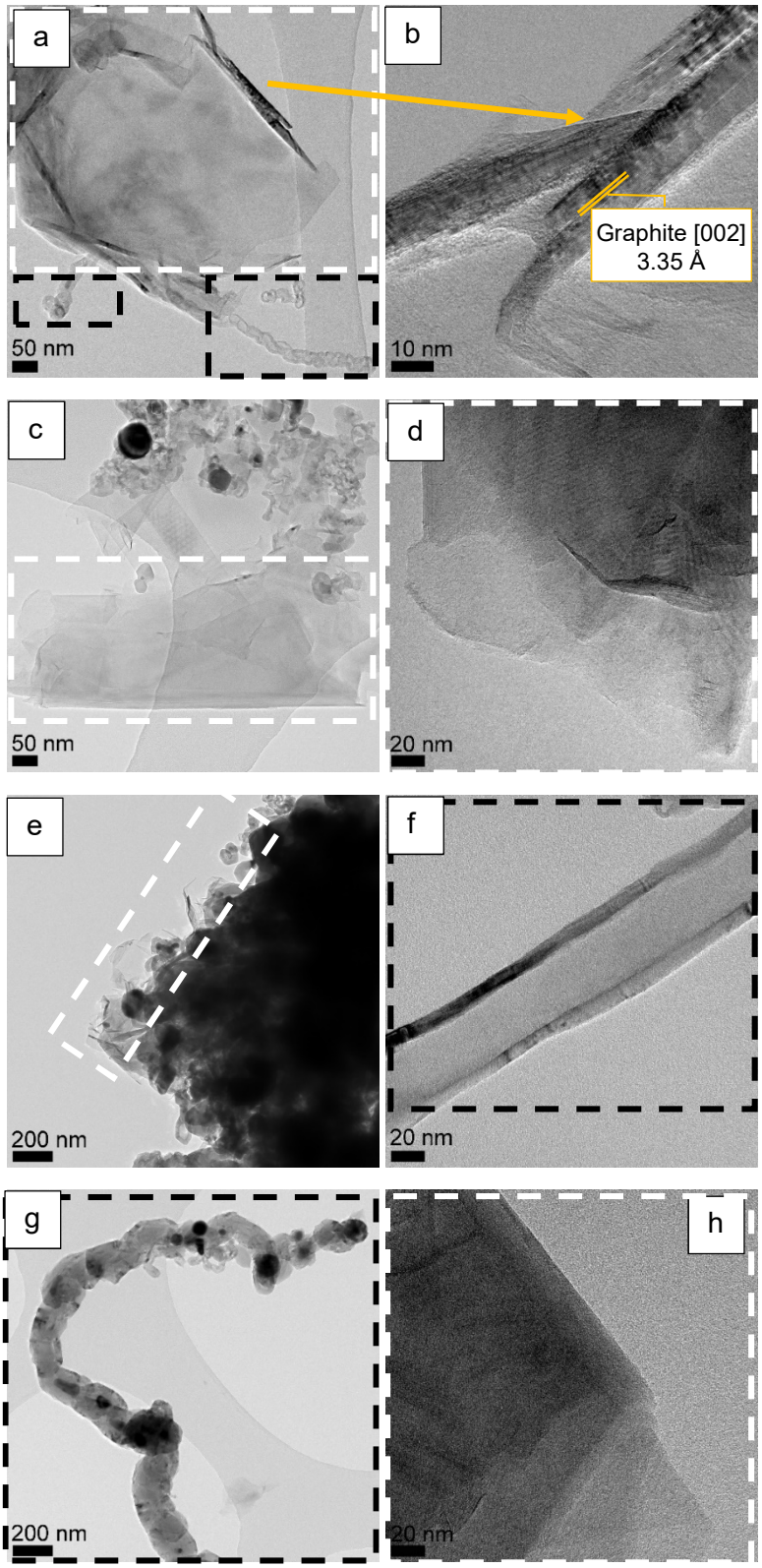

Figure 8 - TEM images of spent samples: (a-b) Tierga-$CH_4$800, (c-d) Tierga-$H_2$800, (e-f) Tierga-$CH_4$900, (g-h) Tierga$H_2$900.

International Journal of Hydrogen Energy 46(71): 35137-35148 (2021)
http://dx.doi.org/10.1016/j.ijhydene.2021.08.065 © 2021. This manuscript version is made available under the CC-BY-NC-ND 4.0 license https://creativecommons.org/licenses/by-nc-nd/4.0/

The nanocarbon structures such as GNSs and carbon nanofilaments observed in this work can be explained by the quasi-liquid state theory [16,20]. According to some studies [50,51], iron species in the quasi-liquid state combined with the absence of support can produce GNS. Iron-based species with low dispersion and large particles when in quasi-liquid state elongate and expand to form a thin film composed of metal and carbide metal [51]. This film is capable of allowing the dissolution, precipitation of carbon and growth of graphene or graphite sheets on its surface [51]. The formation and growth of short carbon nanotubes and chain-type carbon nanofibers observed in the TEM images may have happened analogously. We can infer that the segregation of the active phase during the reaction enabled the formation and growth of these carbons, as also noticed in some previous works [51,52]. The carbon was precipitated out from the smallest metallic iron particle supersaturated with carbon. The growth occurs in a cylindrical shape and extends to maintain the void inside the tube [7,20,33]. With its growth, the interface between the carbon and metal walls decreases and the insertion of the metallic particle into the tube or chain may occur during this process, thus forming the carbon nanotube or chain-type carbon nanofibers [7,20,33].

Raman spectra of the as-deposited carbon nanostructures over the Tierga catalysts are presented in Figure S3. In the Raman first-order spectra (1100 and 1700 cm^{-1}) of the materials, it is possible to observe the characteristic peaks of disordered graphite including D, G, D' at 1350, 1580 and 1620 cm^{-1} respectively. The second-order (2500-3300 cm^{-1}) is the result of overtones and combinations of the bands in the first order, and for the studied materials, peaks were observed in approximately 2450, 2720 and 3240 cm^{-1}, which are attributed to the first overtone of bands at 1220, 1350, 1620 cm^{-1}, and the band 2950 cm^{-1} is a combination of band G and D. The 2D band (~ 2700 cm^{-1}) is characteristic of structures with few and multiple layers of graphene and graphite. Analogous spectra are found in the literature for multilayer graphene and graphite [53].

The integral intensity ratio I_D/I_G is widely used to express the degree of graphitization for the carbon, i.e. the lower I_D/I_G ratio, the higher crystalline order of the carbon species. The

International Journal of Hydrogen Energy 46(71): 35137-35148 (2021)
http://dx.doi.org/10.1016/j.ijhydene.2021.08.065 © 2021. This manuscript version is made available under the CC-BY-NC-ND 4.0 license https://creativecommons.org/licenses/by-nc-nd/4.0/
average parameters of the spectra are shown in Table 3. The I_D/I_G values of all samples were all below 1 (Table 3), which means that the carbon is ordered, with minor contributions from disordered particles.

The low I_D/I_G value corroborates TEM images, showing that the carbon nanostructures were predominantly composed of multilayer graphene or graphite nanosheets and small quantities of nanofilaments. The results presented in this work agreed well with other studies in which low I_D/I_G was favored when the final product was multilayer graphene flakes, high temperatures, and flows of pure methane [36,54,55]. Compared to synthetic pure Fe_2O_3 reported in the literature [14], Tierga generated hybrid carbon with fewer defects and a higher amount of carbon. The materials showed I_D/I_G results close at the same reaction temperature (Table 3), however, the most significant difference was between the materials Tierga-$CH_4$800 and Tierga-$H_2$800. The I_D/I_G value was 0.19 for Tierga-$CH_4$800 and 0.25 for Tierga-$H_2$800, which means that the material Tierga-$CH_4$800 was nanostructured with fewer defects than Tierga-$H_2$800. These same materials showed the greatest difference in carbon yield, 1.05 g_c/g_{cat} for Tierga-$CH_4$800 and 0.82 g_c/g_{cat} Tierga-$H_2$800. This result is in concordance with previous studies [56] which suggested that one of the conditions for carbon growth is preventing disordered the carbon formation. The quality of produced carbon depended on the catalyst treatment and interestingly the results were better with the treatment of the catalyst with CH_4 which is an advantage in the development of the CDM industrial process.

Finally, TPO was performed to evaluate the thermal stability of the spent Tierga catalysts (Figure 9). In all profiles, it is first observed that there was a slight gain in mass close to 450 °C, which may be related to the oxidation of the metallic iron and iron carbide phases located on the surface, followed by a sharp decay in mass between 600 and 630 °C. The higher the reaction temperature, the greater the displacement of the oxidation temperature to higher temperatures. This result is consistent with what was observed in Raman and TEM, which indicates a highly ordered crystal structures (500-700 °C) with the absence of amorphous carbon (~ 400 °C).

International Journal of Hydrogen Energy 46(71): 35137-35148 (2021)
http://dx.doi.org/10.1016/j.ijhydene.2021.08.065 © 2021. This manuscript version is made available under the CC-BY-NC-ND 4.0 license https://creativecommons.org/licenses/by-nc-nd/4.0/

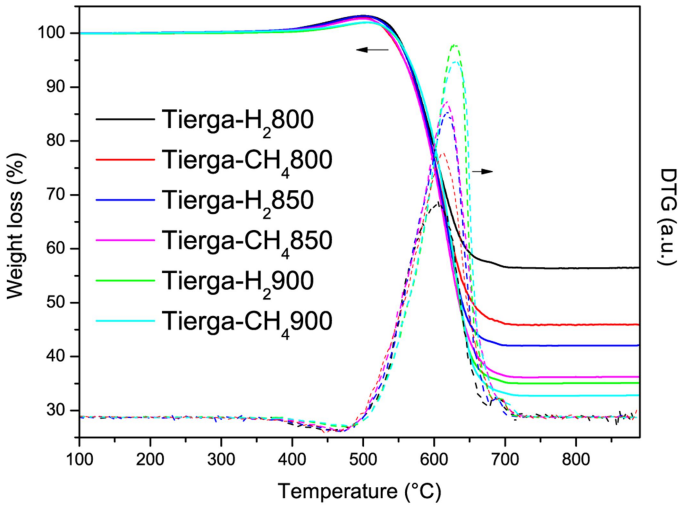

Figure 9 - TPO profiles for spent Tierga catalysts.

4. Conclusions

Tierga and Ilmenite were confirmed as an active catalyst in the production of CO_2-free H_2 and carbon. However, Tierga showed significantly higher catalytic results than Ilmenite and was therefore further investigated. The methane conversion and hydrogen concentration over Tierga were 56% and 70%, respectively, after 3 hours of reaction. Tierga reduced with CH_4 demonstrated superior performance with greater activity and stability than Tierga pretreated with H_2 at moderate temperatures. CH_4 activation has contributed to the fragmentation of the active phase α-Fe which led to smaller crystallites preventing agglomeration and sintering. Such characteristics also promoted the formation of γ-Fe rather than Fe_3C. The high stability of Tierga can be primarily associated with a high degree of graphitization. At 900 °C, there were no significant differences between the Tierga materials in terms of the conversion and reaction mechanism, however, the deactivation started after a certain time, which is related to the encapsulation of chain-like carbon nanofibers. XRD, TEM and Raman revealed the production of structures with nanosheets of graphite and carbon nanotube structures with a high degree of graphitization. WHSV and reaction temperature play a central role in the stability of this material as well, in which the optimal conditions were 2 L/(g_{cat}·h) and 850 °C. The use of iron ore as a natural and low-cost catalyst in the production of nanocarbon structures can contribute as an alternative to assessing the practical use of the CDM process.

International Journal of Hydrogen Energy 46(71): 35137-35148 (2021)
http://dx.doi.org/10.1016/j.ijhydene.2021.08.065 © 2021. This manuscript version is made available under the CC-BY-NC-ND 4.0 license https://creativecommons.org/licenses/by-nc-nd/4.0/

Acknowledgments

Brazilian funding to support this work was provided by CNPq [Process 141308/2018-4], FAPESP [Process 2018/01258-5], CAPES [Finance Code 001]. Spanish funding was provided by the European Regional Development Fund and the Spanish Economy and Competitiveness Ministry (MINECO) [ENE2017-83854-R]. Authors would like to acknowledge the use of "Servicio General de Apoyo a la Investigación-SAI, Universidad de Zaragoza". The authors also thank PROMINDSA and Titania A/S for providing the iron ore used in this work.

Competing interests

The authors declare no competing interests.

References

[1] Muradov N. Low to near-zero CO_2 production of hydrogen from fossil fuels: Status and perspectives. Int J Hydrogen Energy 2017;42:14058–88. https://doi.org/10.1016/j.ijhydene.2017.04.101.

[2] Keipi T, Tolvanen H, Konttinen J. Economic analysis of hydrogen production by methane thermal decomposition: Comparison to competing technologies. Energy Convers Manag 2018;159:264–73. https://doi.org/10.1016/j.enconman.2017.12.063.

[3] Qian JX, Chen TW, Enakonda LR, Liu D Bin, Basset JM, Zhou L. Methane decomposition to pure hydrogen and carbon nano materials: State-of-the-art and future perspectives. Int J Hydrogen Energy 2020;45:15721–43. https://doi.org/10.1016/j.ijhydene.2020.04.100.

[4] Wang IW, Kutteri DA, Gao B, Tian H, Hu J. Methane Pyrolysis for Carbon Nanotubes and CO_x-Free H_2 over Transition-Metal Catalysts. Energy and Fuels 2019;33:197–205. https://doi.org/10.1021/acs.energyfuels.8b03502.

[5] Chen D, Christensen KO, Ochoa-Fernández E, Yu Z, Tøtdal B, Latorre N, et al. Synthesis of carbon nanofibers: Effects of Ni crystal size during methane decomposition.

http://dx.doi.org/10.1016/j.ijhydene.2021.08.065 © 2021. This manuscript version is made available under the CC-BY-NC-ND 4.0 license https://creativecommons.org/licenses/by-nc-nd/4.0/

J Catal 2005;229:82–96. https://doi.org/10.1016/j.jcat.2004.10.017.

[6] Awadallah AE, Aboul-Enein AA, Kandil UF, Taha MR. Facile and large-scale synthesis of high quality few-layered graphene nano-platelets via methane decomposition over unsupported iron family catalysts. Mater Chem Phys 2017;191:75–85. https://doi.org/10.1016/j.matchemphys.2017.01.007.

[7] Li Y, Li D, Wang G. Methane decomposition to CO_x-free hydrogen and nano-carbon material on group 8-10 base metal catalysts: A review. Catal Today 2011;162:1–48. https://doi.org/10.1016/j.cattod.2010.12.042.

[8] Karaismailoğlu M, Figen HE, Baykara SZ. Methane decomposition over Fe-based catalysts. Int J Hydrogen Energy 2020;45:34773–82. https://doi.org/10.1016/j.ijhydene.2020.07.219.

[9] Wang D, Zhang J, Sun J, Gao W, Cui Y. Effect of metal additives on the catalytic performance of Ni/Al_2O_3 catalyst in thermocatalytic decomposition of methane. Int J Hydrogen Energy 2019;44:7205–15. https://doi.org/10.1016/j.ijhydene.2019.01.272.

[10] Tezel E, Figen HE, Baykara SZ. Hydrogen production by methane decomposition using bimetallic Ni–Fe catalysts. Int J Hydrogen Energy 2019;44:9930–40. https://doi.org/10.1016/j.ijhydene.2018.12.151.

[11] Karimi S, Bibak F, Meshkani F, Rastegarpanah A, Deng J, Liu Y, et al. Promotional roles of second metals in catalyzing methane decomposition over the Ni-based catalysts for hydrogen production: A critical review. Int J Hydrogen Energy 2021;46:20435–80. https://doi.org/10.1016/j.ijhydene.2021.03.160.

[12] Ramasubramanian V, Ramsurn H, Price GL. Hydrogen production by catalytic decomposition of methane over Fe based bi-metallic catalysts supported on CeO_2–ZrO_2. Int J Hydrogen Energy 2020;45:12026–36. https://doi.org/10.1016/j.ijhydene.2020.02.170.

[13] Torres D, Pinilla JL, Suelves I. Cobalt doping of α-Fe/Al_2O_3 catalysts for the production of hydrogen and high-quality carbon nanotubes by thermal decomposition of methane. Int J Hydrogen Energy 2020;45:19313–23.

http://dx.doi.org/10.1016/j.ijhydene.2021.08.065 © 2021. This manuscript version is made available under the CC-BY-NC-ND 4.0 license https://creativecommons.org/licenses/by-nc-nd/4.0/

https://doi.org/10.1016/j.ijhydene.2020.05.104.

[14] Pudukudy M, Kadier A, Yaakob Z, Takriff MS. Non-oxidative thermocatalytic decomposition of methane into COx free hydrogen and nanocarbon over unsupported porous NiO and Fe_2O_3 catalysts. Int J Hydrogen Energy 2016;41:18509–21. https://doi.org/10.1016/j.ijhydene.2016.08.160.

[15] Shaikhutdinov SK, Zaikovskii VI, Avdeeva LB. Coprecipitated Ni-alumina and Ni-Cu-alumina catalysts of methane decomposition and carbon deposition III. Morphology and surface structure of the carbon filaments. Appl Catal A Gen 1996;148:123–33. https://doi.org/10.1016/S0926-860X(96)00226-8.

[16] Schaper AK, Hou H, Greiner A, Phillipp F. The role of iron carbide in multiwalled carbon nanotube growth. J Catal 2004;222:250–4. https://doi.org/10.1016/j.jcat.2003.11.011.

[17] Deck CP, Vecchio K. Prediction of carbon nanotube growth success by the analysis of carbon-catalyst binary phase diagrams. Carbon N Y 2006;44:267–75. https://doi.org/10.1016/j.carbon.2005.07.023.

[18] Qian JX, Chen TW, Enakonda LR, Liu D Bin, Mignani G, Basset JM, et al. Methane decomposition to produce CO_x-free hydrogen and nano-carbon over metal catalysts: A review. Int J Hydrogen Energy 2020;45:7981–8001. https://doi.org/10.1016/j.ijhydene.2020.01.052.

[19] Sikander U, Samsudin MF, Sufian S, KuShaari KZ, Kait CF, Naqvi SR, et al. Tailored hydrotalcite-based Mg-Ni-Al catalyst for hydrogen production via methane decomposition: Effect of nickel concentration and spinel-like structures. Int J Hydrogen Energy 2019;44:14424–33. https://doi.org/10.1016/j.ijhydene.2018.10.224.

[20] Ermakova MA, Ermakov DY, Chuvilin AL, Kuvshinov GG. Decomposition of methane over iron catalysts at the range of moderate temperatures: The influence of structure of the catalytic systems and the reaction conditions on the yield of carbon and morphology of carbon filaments. J Catal 2001;201:183–97. https://doi.org/10.1006/jcat.2001.3243.

[21] Pudukudy M, Yaakob Z, Mazuki MZ, Takriff MS, Jahaya SS. One-pot sol-gel synthesis

http://dx.doi.org/10.1016/j.ijhydene.2021.08.065 © 2021. This manuscript version is made available under the CC-BY-NC-ND 4.0 license https://creativecommons.org/licenses/by-nc-nd/4.0/

of MgO nanoparticles supported nickel and iron catalysts for undiluted methane decomposition into CO_x free hydrogen and nanocarbon. Appl Catal B Environ 2017;218:298–316. https://doi.org/10.1016/j.apcatb.2017.04.070.

[22] Pinilla JL, Utrilla R, Lázaro MJ, Suelves I, Moliner R, Palacios JM. A novel rotary reactor configuration for simultaneous production of hydrogen and carbon nanofibers. Int J Hydrogen Energy 2009;34:8016–22. https://doi.org/10.1016/j.ijhydene.2009.07.057.

[23] Inaba M, Zhang Z, Matsuoka K, Soneda Y. Optimization of the reaction conditions for Fe-catalyzed decomposition of methane and characterization of the produced nanocarbon fibers. Catal Today 2019;332:11–9. https://doi.org/10.1016/j.cattod.2018.11.014.

[24] Qian JX, Enakonda LR, Wang WJ, Gary D, Del-Gallo P, Basset JM, et al. Optimization of a fluidized bed reactor for methane decomposition over Fe/Al_2O_3 catalysts: Activity and regeneration studies. Int J Hydrogen Energy 2019;44:31700–11. https://doi.org/10.1016/j.ijhydene.2019.10.058.

[25] Enakonda LR, Zhou L, Saih Y, Ould-Chikh S, Lopatin S, Gary D, et al. Methane-induced activation mechanism of fused ferric oxide–alumina catalysts during methane decomposition. ChemSusChem 2016;9:1911–5. https://doi.org/10.1002/cssc.201600500.

[26] Abad A, Mendiara T, de Diego LF, García-Labiano F, Gayán P, Adánez J. A simple model for comparative evaluation of different oxygen carriers and solid fuels in iG-CLC processes. Fuel Process Technol 2018;179:444–54. https://doi.org/10.1016/j.fuproc.2018.07.031.

[27] Mendiara T, Abad A, de Diego LF, García-Labiano F, Gayán P, Adánez J. Reduction and oxidation kinetics of Tierga iron ore for Chemical Looping Combustion with diverse fuels. Chem Eng J 2019;359:37–46. https://doi.org/10.1016/j.cej.2018.11.022.

[28] Pudukudy M, Yaakob Z, Jia Q, Takriff MS. Catalytic decomposition of methane over rare earth metal (Ce and La) oxides supported iron catalysts. Appl Surf Sci 2019;467–468:236–48. https://doi.org/10.1016/j.apsusc.2018.10.122.

[29] Torres D, Pinilla JL, Lázaro MJ, Moliner R, Suelves I. Hydrogen and multiwall carbon

nanotubes production by catalytic decomposition of methane: Thermogravimetric analysis and scaling-up of Fe-Mo catalysts. Int J Hydrogen Energy 2014;39:3698–709. https://doi.org/10.1016/j.ijhydene.2013.12.127.

[30] Awadallah AE, Abdel-Mottaleb MS, Aboul-Enein AA, Yonis MM, Aboul-Gheit AK. Catalytic Decomposition of Natural Gas to CO/CO_2-Free Hydrogen Production and Carbon Nanomaterials Using MgO-Supported Monometallic Iron Family Catalysts. Chem Eng Commun 2015;202:163–74. https://doi.org/10.1080/00986445.2013.836631.

[31] Tang L, Yamaguchi D, Burke N, Trimm D, Chiang K. Methane decomposition over ceria modified iron catalysts. Catal Commun 2010;11:1215–9. https://doi.org/10.1016/j.catcom.2010.07.004.

[32] Zieliński J, Zglinicka I, Znak L, Kaszkur Z. Reduction of Fe_2O_3 with hydrogen. Appl Catal A Gen 2010;381:191–6. https://doi.org/10.1016/j.apcata.2010.04.003.

[33] Zhou L, Enakonda LR, Harb M, Saih Y, Aguilar-Tapia A, Ould-chikh S, et al. Fe catalysts for methane decomposition to produce hydrogen and carbon nano materials. Appl Catal B, Environ 2017;208:44–59. https://doi.org/10.1016/j.apcatb.2017.02.052.

[34] Abad A, Adánez J, Cuadrat A, García-Labiano F, Gayán P, de Diego LF. Kinetics of redox reactions of ilmenite for chemical-looping combustion. Chem Eng Sci 2011;66:689–702. https://doi.org/10.1016/j.ces.2010.11.010.

[35] García-Muñoz P, Pliego G, Zazo JA, Barbero B, Bahamonde A, Casas JA. Modified ilmenite as catalyst for CWPO-Photoassisted process under LED light. Chem Eng J 2017;318:89–94. https://doi.org/10.1016/j.cej.2016.05.093.

[36] Jana P, O'Shea VAD, Coronado JM, Serrano DP. Co-production of graphene sheets and hydrogen by decomposition of methane using cobalt based catalysts. Energy Environ Sci 2011;4:778–83. https://doi.org/10.1039/c0ee00490a.

[37] Li Y, Zhao C, Duan L, Liang C, Li Q, Zhou W, et al. Cyclic calcination/carbonation looping of dolomite modified with acetic acid for CO_2 capture. Fuel Process Technol 2008;89:1461–9. https://doi.org/10.1016/j.fuproc.2008.07.008.

[38] Lachén J, Plou J, Durán P, Herguido J, Peña JA. Iron oxide ores as carriers for the

production of high purity hydrogen from biogas by steam–iron process. Int J Hydrogen Energy 2017;42:13607–16. https://doi.org/10.1016/j.ijhydene.2016.11.152.

[39] Pudukudy M, Yaakob Z. Methane decomposition over Ni, Co and Fe based monometallic catalysts supported on sol gel derived SiO_2 microflakes. Chem Eng J 2015;262:1009–21. https://doi.org/10.1016/j.cej.2014.10.077.

[40] Pinilla JL, Lázaro MJ, Suelves I, Moliner R. Formation of hydrogen and filamentous carbon over a Ni-Cu-Al_2O_3 catalyst through ethane decomposition. Appl Catal A Gen 2011;394:220–7. https://doi.org/10.1016/j.apcata.2011.01.005.

[41] Lua AC, Wang HY. Decomposition of methane over unsupported porous nickel and alloy catalyst. Appl Catal B, Environ 2013;132–133:469–78. https://doi.org/10.1016/j.apcatb.2012.12.014.

[42] Zardin L, Perez-Lopez OW. Hydrogen production by methane decomposition over Co-Al mixed oxides derived from hydrotalcites: Effect of the catalyst activation with H_2 or CH_4. Int J Hydrogen Energy 2017;42:7895–907. https://doi.org/10.1016/j.ijhydene.2017.02.153.

[43] Guo Z, Zheng JE, Liu Y, Chu W. Insight into the role of metal/oxide interaction and Ni availabilities on NiAl mixed metal oxide catalysts for methane decomposition. Appl Catal A Gen 2018;555:1–11. https://doi.org/10.1016/j.apcata.2018.01.031.

[44] Jiang DE, Carter EA. Carbon dissolution and diffusion in ferrite and austenite from first principles. Phys Rev B - Condens Matter Mater Phys 2003;67:1–11. https://doi.org/10.1103/PhysRevB.67.214103.

[45] Takenaka S, Serizawa M, Otsuka K. Formation of filamentous carbons over supported Fe catalysts through methane decomposition. J Catal 2004;222:520–31. https://doi.org/10.1016/j.jcat.2003.11.017.

[46] Häglund J, Fernndez Guillermet A, Grimvall G, Körling M. Theory of bonding in transition-metal carbides and nitrides. Phys Rev B 1993;48:11685–91. https://doi.org/10.1103/PhysRevB.48.11685.

[47] Wirth CT, Bayer BC, Gamalski AD, Esconjauregui S, Weatherup RS, Ducati C, et al.

http://dx.doi.org/10.1016/j.ijhydene.2021.08.065 © 2021. This manuscript version is made available under the CC-BY-NC-ND 4.0 license https://creativecommons.org/licenses/by-nc-nd/4.0/

The phase of iron catalyst nanoparticles during carbon nanotube growth. Chem Mater 2012;24:4633–40. https://doi.org/10.1021/cm301402g.

[48] Jourdain V, Bichara C. Current understanding of the growth of carbon nanotubes in catalytic chemical vapour deposition. Carbon N Y 2013;58:2–39. https://doi.org/10.1016/j.carbon.2013.02.046.

[49] Wang HY, Lua AC. Methane decomposition using Ni-Cu alloy nano-particle catalysts and catalyst deactivation studies. Chem Eng J 2015;262:1077–89. https://doi.org/10.1016/j.cej.2014.10.063.

[50] El-Ahwany OM, Awadallah AE, Aboul-Enein AA, Abdel-Azim SM, Aboul-Gheit NAK, Abo-EL-Enein SA. Dual growth of graphene nanoplatelets and carbon nanotubes hybrid structure via chemical vapor deposition of methane over Fe–MgO catalysts. Fullerenes Nanotub Carbon Nanostructures 2019;28:435–45. https://doi.org/10.1080/1536383X.2019.1697243.

[51] Aboul-Enein AA, Awadallah AE. Production of nanostructured carbon materials using Fe–Mo/MgO catalysts via mild catalytic pyrolysis of polyethylene waste. Chem Eng J 2018;354:802–16. https://doi.org/10.1016/j.cej.2018.08.046.

[52] Awadallah AE, El-Desouki DS, Aboul-Gheit NAK, Ibrahim AH, Aboul-Gheit AK. Effect of crystalline structure and pore geometry of silica based supported materials on the catalytic behavior of metallic nickel particles during methane decomposition to CO_x-free hydrogen and carbon nanomaterials. Int J Hydrogen Energy 2016;41:16890–902. https://doi.org/10.1016/j.ijhydene.2016.07.081.

[53] Gupta A, Chen G, Joshi P, Tadigadapa S, Eklund PC. Raman scattering from high-frequency phonons in supported n-graphene layer films. Nano Lett 2006;6:2667–73. https://doi.org/10.1021/nl061420a.

[54] Son SY, Lee Y, Won S, Lee DH, Kim SD, Sung SW. High-quality multiwalled carbon nanotubes from catalytic decomposition of carboneous materials in gas-solid fluidized beds. Ind Eng Chem Res 2008;47:2166–75. https://doi.org/10.1021/ie0711630.

[55] Jin Y, Wang G, Li Y. Catalytic growth of high quality single-walled carbon nanotubes

International Journal of Hydrogen Energy 46(71): 35137-35148 (2021)
http://dx.doi.org/10.1016/j.ijhydene.2021.08.065 © 2021. This manuscript version is made available under the CC-BY-NC-ND 4.0 license https://creativecommons.org/licenses/by-nc-nd/4.0/

over a Fe/MgO catalyst derived from a precursor containing Feitknecht compound. Appl Catal A Gen 2012;445–446:121–7. https://doi.org/10.1016/j.apcata.2012.08.010.

[56] Harutyunyan AR, Mora E, Tokune T, Bolton K, Rosén A, Jiang A, et al. Hidden features of the catalyst nanoparticles favorable for single-walled carbon nanotube growth. Appl Phys Lett 2007;90:163120. https://doi.org/10.1063/1.2730730.